Ab initio calculations of the rate of carrier trapping and release at dopant sites in NaI: Tl beyond the harmonic approximation

Micah P. Prange, Niranjan Govind, and Sebastien N. Kerisit

Ab initio calculations of the rate of carrier trapping and release at dopant sites in NaI:Tl beyond the harmonic approximation

Micah P. Prange,[†][*] Niranjan Govind,[§] and Sebastien N. Kerisit[†]

[†]Physical Sciences Division, Physical and Computational Sciences Directorate, Pacific Northwest National Laboratory, Richland, Washington 99354, United States

[§]Environmental Molecular Sciences Division, Earth and Biological Sciences Directorate, Pacific Northwest National Laboratory, Richland, Washington 99354, United States

[*]Corresponding author: micah.prange@pnnl.gov.

ABSTRACT

We present ab initio calculations of electron capture and release coefficients as a function of temperature for Tl dopants in the widely used scintillator NaI, which is a soft ionic crystal. The modelled capture and release events occur by transitions mediated by multiple phonon absorption and emission between states with significantly different local geometries around the trapping site. We demonstrate that such transitions are not well-described by the normal harmonic approximation to the nuclear dynamics. We go beyond the harmonic approximation by numerically solving the vibrational Schrödinger equation for the motion along/of a single effective phonon coordinate. The localized trapped state is not correctly described by semilocal density functionals, so we employ a global hybrid functional tuned to reproduce the band gap and lattice constant of the host material. Our calculations, which combine plane-wave and embedded cluster electronic structure methods in a novel way, are in reasonable agreement with available experimental data for detrapping and predict an unusual temperature dependence for trapping rates.

I.   INTRODUCTION

Thallium-doped sodium iodide (NaI:Tl) is the most used inorganic scintillator material [1] with a long history of many important applications [2]. The alkali halide salts exhibit large electron-phonon interaction and correspondingly interesting optical properties that have attracted a long history of study by laser spectroscopy [3-13]. In the last decade, demand for improved gamma-ray detection systems has driven renewed interest in the scintillation mechanisms in alkali halide and related material systems [14-36]. Despite this considerable history of research, there are still many open questions regarding the complicated sequence of events following gamma excitation, which involves many excitations coupling defects, lattice deformations, and electronic excitations.

A scintillator emits optical light after ionizing radiation deposits energy in the crystal, resulting in one to several highly energetic electrons and matching holes. These primary excitations in turn create secondary electrons and holes in an energy cascade. The timing and amount of emitted light is determined by the radiative recombination of these excitations—each recombination emits an optical photon. The energy of the original ionizing radiation quantum (gamma ray, electron, alpha particle, etc.) is then inferred from the total amount (time-integrated intensity) of emitted light. Hence the response time, brightness, and ultimate energy resolution achievable in radiation detectors based on scintillation is determined by the dynamics of electron-hole recombination. Quantitative models of scintillation, then, need to account for the processes that determine the likelihood and time scales of radiative recombination. These quantities are determined by the collective motion of the electrons and holes, including self-

1

trapping and trapping and release from activators. Progress has been made recently, driven by improved time-resolved optical spectroscopy, in the development of microscopic models of radiation transport following gamma excitation. This new research has increased knowledge of the photophysics to the point of quantitative knowledge of the types and populations of different excitation species including electronically excited activators (impurities) [37], charged and neutral self-trapped electronic excitations [26], and free electron-hole pairs [18,20,38] in a few systems.

In this work we examine the case of a Tl activator in a NaI crystal. In the ground state, Tl exists in a +1 charge state as an isovalent substituent of Na in the NaI rock-salt structure. After gamma excitation, the Tl^+ sites can trap both holes ($Tl^+ + h^+ \rightarrow Tl^{++}$) and electrons ($Tl^+ + e^- \rightarrow Tl^0$). Tl^+ can also trap neutral triplet excitons, resulting in an excited species we label Tl^* that decays radiatively producing the scintillation light. Tl^* can also be formed by sequential trapping of carriers of opposite sign (e.g. $Tl^0 + h^+ \rightarrow Tl^*$). This knowledge comes from a long history of models posited initially to explain the observed optical properties of self-trapped holes [4-7]. These models were later extended in an effort to quantitatively describe the fundamental limits imposed on radiation detection systems by intrinsic properties of the scintillating crystal [16,18,23,26,33]. Insights gained from these models and other theoretical work [37,39-41] include the realization that carrier trapping plays a key role in many aspects of scintillation including limiting the achievable energy resolution for high-energy gamma-ray spectroscopy. Understanding of carrier trapping dynamics is also a prerequisite for cogent material design. For example, much effort has been expended trying to improve scintillator performance by codoping [42-50]. To date, these efforts have been largely empirical since a lack of detailed knowledge of the relative trapping rates at different dopant sites precludes the development of serious working

hypotheses regarding the mechanisms by which performance might be improved by the introduction of new traps. Holes quickly self-trap in alkali halides [9] if they do not trap on activators. Afterward, they move diffusively. Electrons, on the other hand, do not self-trap in NaI. Instead they travel ballistically away from the ionization track until they are drawn back by electrostatic attraction to the positively charged track core. To participate in luminescence, these electrons must end up at an activator site along with a hole. Competition between different types of traps, then, determines the population of electrons available for radiative recombination. Hence, the electron trapping (and release) dynamics represent a key source of uncertainty in the current generation of scintillation models. This work is an attempt to fill this knowledge gap using electronic structure calculations. Recent work using thermally stimulated luminescence [51] provides some experimental data regarding electron release from Tl in NaI:Tl. For these reasons we have chosen to study electron trapping and detrapping from Tl sites in NaI:Tl theoretically. We do this by using and extending electronic structure approaches to inelastic electron scattering by phonons[52,53] to simulate the vibrational dynamics around Tl in NaI:Tl and the probability that these vibrations cause an electron to be trapped or released by multi-phonon processes.

II.   THEORETICAL FRAMEWORK and DEFINITION OF TERMS

The history of inelastic electron scattering by multi-phonon emission has recently been nicely reviewed in the introduction of a paper by Barmparis et al. [53]. Shi et al. have recently compared different numerical formalisms in this area [54,55]. The field is seeing increased activity recently, including this work, as electronic structure methods are becoming reliable enough to treat the delicate physics of the electron-phonon interaction. We rely on density functional theory (DFT) in two different implementations: the embedded cluster approach, with

3

orbitals expanded in local atom-centered basis functions, and periodic models based on supercells, with orbitals expanded in plane wave basis sets.

The theoretical framework and numerical approximations used in this manuscript largely follow Alkauskas and coworkers [52] to which we refer the reader for a discussion of the validity of the major approximations and the motivations for choosing them. We will sketch their derivation here and note the differences in our approach, which has been tailored to the softer ionic nature of NaI compared to the semiconductor systems studied in Ref. [52]. Our system of interest is a NaI crystal with a single Tl atom occupying one of the sites on the Na sublattice, and we consider the situation of an extra electron introduced into this system. We start from Fermi's Second Golden Rule for the lifetime τ_{iI} of the quantum state $|iI\rangle$ [56,57].

$$\frac{1}{\tau_{iI}} = \frac{2\pi}{\hbar} \sum_{fF \neq iI} \left| \langle iI | \hat{H}^{ep} | fF \rangle \right|^2 \delta\left(E_{iI} - E_{fF} \right). \tag{1}$$

$\hat{H}^{ep}$ is the electron-phonon interaction Hamiltonian, which Eq. (1) treats to first order [52], E_{iI} is the energy of the state $|iI\rangle$, and $\hbar = h/(2\pi)$ is Planck's reduced constant. There are three aspects of this expression that need to be approximated leading to three distinct types of approximations: the wave-functions of the quantum states of the system must be expressed in a way that matrix elements of $\hat{H}^{ep}$ between them can be evaluated, the energies of the states must be found so that the δ-function can be evaluated, and $\hat{H}^{ep}$ itself must be approximated.

The full quantum state of the system is written as a product state. Lowercase Roman letters refer to electronic states, which depend explicitly on the electron coordinates and implicitly on the nuclear coordinates, capitals to vibrational states which depend explicitly on the nuclear coordinates and implicitly on the electronic state: $|iI\rangle = |i\rangle|I\rangle$. This is the Born-Oppenheimer approximation; if the electronic states used are eigenstates for fixed atomic

coordinates, as in this work, one has the static approximation [58]. We further approximate the electronic states as Slater determinants of Kohn-Sham (KS) orbitals; then $\hat{H}^{ep}$ connects states that differ by at most one orbital. Note that at least one of the electronic states is not the ground state, so there is an implicit independent-particle approximation (i.e. excited state effects are neglected by using ground-state Kohn-Sham orbitals and eigenvalues) at this stage. The energies E_{iI} of the states are similarly taken to be the sum of electronic and vibrational energies. The former is estimated using DFT calculations that give the orbitals, the details of which are given below. The latter are computed in a one-dimensional approximation in which a single effective phonon coordinate Q mediates the transition of interest [52] (in our case the capture or release of an electron from a Tl dopant). This is a major approximation that reduces the high-dimensional phonon problem to a soluble 1-D problem and permits a key advance of the current work: the avoidance of the harmonic approximation. The use of an effective 1-D phonon space has been tested by Alkauskas et al. [59]. The nuclear dynamics are then determined (separately for each electronic state) by the 1-D Schrödinger equation for a particle moving on an adiabatic potential energy surface (PES) computed within DFT in a given electronic configuration. Hence the (1-D) vibrational wave functions depend on the electronic state. Within this framework, linearizing the electron-phonon interaction Hamiltonian (not the effective PES) in Q around $Q = Q_0$ gives the total electron-phonon matrix element in the form

$$\langle iI|\hat{H}^{ep}|fF\rangle = \left\langle i\left|\frac{\partial \hat{H}^{ep}}{\partial Q}\right|f\right\rangle \langle I|Q - Q_0|F\rangle = W_{if}\langle I|Q - Q_0|F\rangle. \tag{2}$$

The electronic part is further approximated

$$W_{if} = \left(\epsilon_f - \epsilon_i\right)\left\langle i\left|\frac{\partial f}{\partial Q}\right\rangle = \left(\epsilon_f - \epsilon_i\right)\frac{\partial}{\partial Q}\langle i(Q = Q_0)|f(Q)\rangle. \tag{3}$$

As indicated, the derivative is evaluated at $Q=Q_0$, consistent with the static approximation. The effective vibrational coordinate is related to locations of the atoms by [52]

$$Q^2 = \sum_l m_l \left(\vec{R}_l - \vec{R}_{0l}\right)^2. \tag{4}$$

where m_l and $\vec{R}_l$ are respectively the mass and position of the atom at site l, $\vec{R}_{0l}$ is the position of the atom at site l in a reference state corresponding to $Q = Q_0$. The $\vec{R}_{0l}$ and $\vec{R}_l$ are found by minimizing the energy of appropriate supercells or cluster models as described below. The sum runs over the entire crystal, but due to the localized nature of the trapped state, $\vec{R}_l - \vec{R}_{0l}$ tends to $\vec{0}$ as the distance between the lattice site l and the site of the Tl atom grows. In practice, we restrict all sums over l either to the cluster model being used for the electronic structure (when using local basis sets) or the first supercell (when using periodic boundary conditions). Q_0 corresponds to the state at which the expression is evaluated. The choice of Q_0 is discussed in Refs. [52,53]; in this work we choose to evaluate Eq. (3) in the trapped state: $Q_0 = Q_{max}$. Note that Eq. (2) is symmetric with respect to exchange of the initial and final states, but the symmetry is broken by the approximation of Eq. (3), which arbitrarily places the derivative on $|f\rangle$ and not $|i\rangle$. We checked the results presented below by computing $\left(\epsilon_f - \epsilon_i\right)\left\langle i \left| \frac{\partial f}{\partial Q}\right\rangle\right.$ and $\left(\epsilon_i - \epsilon_f\right)\left\langle f \left| \frac{\partial i}{\partial Q}\right\rangle\right.$ for the relevant orbitals (the choice of which is discussed below), finding agreement to better than 0.2%.

To relate estimates of trapping and detrapping time based on Eq. (1) to macroscopic phenomena, we assume the electronic system is in a definite charge state (Tl^+ for trapping, Tl^0 for detrapping) and a thermal population of the vibrational levels of the PES of the charge state. Hence, the final expression for the transition rate R is

$$R = g_i \frac{2\pi}{\hbar} \sum_I w_I^i \sum_F |\langle iI|\hat{H}^{ep}|fF\rangle|^2 \delta(E_{iI} - E_{fF}) \qquad (5)$$

where w_I^i is the Boltzmann occupation factor for the Ith vibrational level of the electronic state i and g_i is the degeneracy of state i. Since there are 8 equivalent [111] directions for the Tl to move when it traps an electron and our double-well treatment of this state accounts for two of these, we set $g = 4$ for the trapped state. The ground state is nondegenerate, so $g = 1$ for the free electron. We further assume bimolecular kinetics for electron trapping (free electrons explore the crystal encountering distributed defects) and unimolecular kinetics for detrapping (each Tl^0 has the same probability to release its electron per unit time). In particular, for a physical sample of volume V containing a concentration of n_{Tl^+} Tl^+ atoms and n_{e^-} free electrons in the conduction band resulting in R_c electron trapping events per unit time per unit volume, we define the capture coefficient C_c by

$$R_c = C_c n_{e^-} n_{\text{Tl}^+} \qquad (6)$$

and, similarly, the release rate per Tl^0 C_r by

$$R_r = C_r n_{\text{Tl}^0} \qquad (7)$$

where n_{Tl^0} is the concentration of Tl atoms that host trapped electrons. Hence below we calculate the rates in specific model systems containing a single Tl site in a given volume and a single extra electron. From the resulting rates we derive C_c and C_r. Alkauskas [52] further includes corrections that account for the modification of the extended (free) states by a charged defect. In the present case, we neglect these corrections since the Tl^+ dopant is an isovalent substituent for the Na^+, and the long-range Coulombic interaction between free e^- and Tl^+ is similar to that

between free e⁻ and Na⁺. Hence we expect 'free' electron states calculated in Tl-containing models to be fair representations of electron dynamics in the actual material.

III.   METHODS and APPROXIMATIONS

To calculate the potential energy surface (configuration-coordinate diagram or cc-diagram) for the effective 1-D phonon coordinate Q, the electronic transition energy, and the electron-phonon matrix elements we use DFT. Two different formulations are used. The electronic transition energy and cc-diagram are computed with the VASP code [60-63] using a 64-atom model (2×2×2 supercell of the conventional 8-atom halite structure cell with one Na replaced by Tl). All but the valence electrons (1 per Na, 3 per Tl, and 7 per I atom) are pseudized using the projector augmented-wave (PAW) [64,65] method (and standard VASP-provided PAW datasets) allowing us to expand the orbitals in basis sets determined by a 500 eV energy cutoff for each of the 8 k-points composing a regular 2×2×2 grid in the Brillouin zone. During structural relaxations, all atomic coordinates and cell parameters were varied until the forces were less than 10^{-3} eV/Å. Electronic minimizations were converged to 10^{-6} eV. We refer to these calculations as plane-wave models (PWMs). We did not include corrections for the spin-orbit coupling in the valence and conduction band states, which we expect to be weak based on the slowness of the triplet-to-singlet radiative decay of (Tl+)* in NaI:Tl (the radiative lifetime is around 200 ns [33,66,67]). The electron-phonon matrix elements were computed using the NWChem package [68]. These calculations were run for a cluster model (CM), with no periodic boundary conditions, of 136 atoms ($Na_{67}TlI_{68}$) arranged in a roughly spherical shape with radius ~8 Å, centered on the Tl impurity. The initial positions were taken from previous work we have done on NaI[69]. As in that work, we have followed Govind et al. [70] to mimic the Ewald potential due to the remainder of the

crystal not explicitly represented in our CM with an array of point charges occupying lattice sites outside the cluster boundary. During structural relaxations, 42 Na and 42 I atoms (the atoms further than 6 Å from the cluster center) on the exterior of the cluster were held fixed (enforcing the experimental lattice parameter). The remaining 52 atoms were fully relaxed. The convergence criteria were set (in atomic units) to 10^{-5}, 10^{-5}, and $10^{-3}/2$ for the energy, density, and gradients, respectively. CRENBL ECP basis sets [71-73] for Na and I sites, and Stuttgart RLC basis sets[73] for Tl, were used. Effective core potentials were used to pseudize all but the valence electrons (9 per Na, 3 per Tl, and 7 per I atom). The CM calculations explicitly included the 2s and 2p Na electrons, while the PWM calculations did not include them.

IV.   RESULTS and DISCUSSION

A.   Parameterization of the exchange-correlation approximation

Semilocal exchange-correlation (xc) approximations will not trap an electron on the Tl site [69], so at least some fraction of non-local exchange is needed to obtain even qualitatively correct behavior. As we will show below, the depth of the electron trap is sensitive to the xc approximation. Hence, the specific choice of xc approximation is a central decision for calculations such as those presented here. We have used the PBE0 [74-76] xc functional, but adjusted the fraction α of explicit exchange [77,78] using the rationale that an xc approximation that "well"-represents the host material NaI is a good starting point for calculating the properties of isolated defects like the Tl_{Na} considered here. Using PWMs of pure NaI (using the primitive cell and converged 8×8×8 k-point grids), we calculated the relaxed lattice parameters and KS

9

gaps (at Γ) for $\alpha = {}^{1}/{}_{n}$, $n = 1,2,3,4,\infty$. The results are summarized in Figure 1, which also

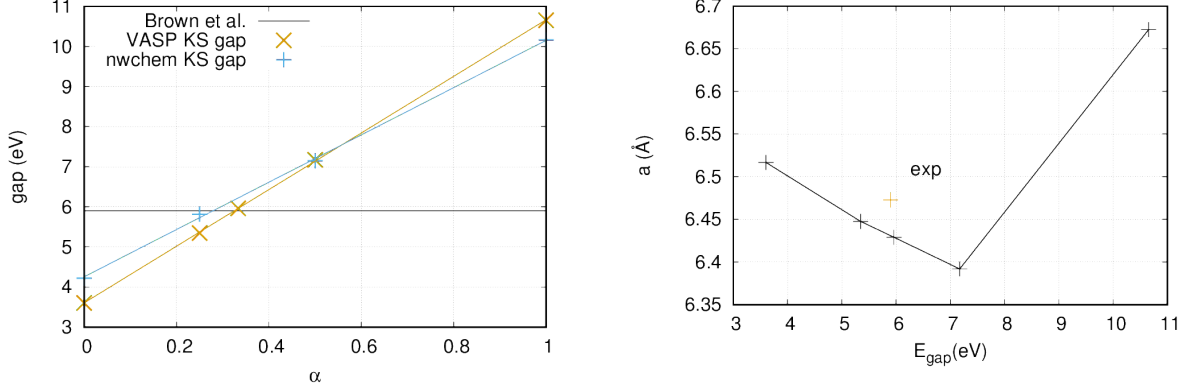displays CM calculations of the KS gap at the fixed, experimental lattice parameter.

Figure 1. Left: Band gap vs. the fraction of explicit exchange included in the xc functional in

our CM (blue) and PWM (yellow) calculations. Right: computed lattice constant a vs. band

gap for the PWM calculations. The experimental band gap is taken from Ref. [79] while the

lattice constant is from Ref. [79,80]. The functionals are otherwise standard PBE for the

remainder of the exchange functional and the correlation functional, except for the case $\alpha = 1$,

which is Hartree-Fock (HF) theory (i.e. no correlation).

The left-hand panel of Figure 1 shows that the predicted KS gap is linear in α with a positive

correlation between the gap and α with semilocal PBE ($\alpha = 0$) exhibiting the DFT gap problem

and $\alpha = 1$ exhibiting unphysically large exchange effects. The measured (at room temperature)

onset of optical transitions to the conduction band [79] (composed primarily of Na s states) is

marked with the black horizontal line. The CM calculations yield a lower slope in the gap vs. α

relation which we attribute to the fixed geometry. We did not attempt to construct CMs at

different lattice constants, but one could do so. The right-hand panel of Figure 1 plots the KS

gaps against the relaxed lattice constant for NaI. Room temperature experimental data are also

shown [80]. Based on these considerations, we chose $\alpha = {}^{1}/{}_{3}$ for the capture and release

calculations presented below; we refer to the resulting xc approximation as PBE0$_{1/3}$. We will describe the combination of xc and cluster type, which we vary frequently in this work, with the notation "xc/cluster type" so that PBE0$_{1/3}$/PWM means a plane-wave model simulated using PBE0$_{1/3}$ (and all the other settings for VASP described above). The PBE0$_{1/3}$/PWM gives a lattice parameter of 6.429 Å (compared to the experimental value of 6.4728 Å [80]) and a KS gap of 5.989 eV (compared to the measured gap [79] of 5.9 eV).

B.   Coordination environment of Tl$^+$ and Tl^0 in NaI and configuration coordinate diagram

Within PBE0$_{1/3}$, we relaxed both CMs and PWMs containing a Tl dopant. As we have found previously [69], the Tl occupies the Na lattice site with a small expansion of its host octahedron (distance between Tl and near-neighbor I is 3.39 Å compared to $^a/_2 = 3.21$ Å Na-I distance in the host material). Below we refer to this structure as the Tl-ground-state structure. To simulate the Tl^0 state we introduced an extra electron. In the PWMs, which employ periodic boundary conditions that preclude a charged cell, the extra charge is compensated by a uniform background charge. We made no further corrections for the electrostatic interactions between the periodic images. We justify this approximation by noting that all energy differences were taken between cells with the same charge and similar dipole moments, so the leading corrections to the electrostatics cancel in the differences. Further, the electrostatic interaction between image charges is screened. With the extra electron, the lowest energy state in PBE0$_{1/3}$/PWM is obtained by displacing the Tl dopant along one of the eight equivalent [111] directions by 0.702 Å (putting the Tl^0 structure at $Q_{max} = 13.53$ amu$^{1/2}$Å with this Tl$^+$ state at $Q = 0$ according to Eq. (4)). The Tl^0 state is 0.242 eV more stable than an extra electron in the Tl-ground-state structure. In PBE0$_{1/3}$/CM, there is a local minimum corresponding to the Tl^0 state, but it is 0.123 eV higher

in energy than the Tl-ground-state structure (of the PBE0$_{1/3}$/CM). The reason for this is that the Tl is displaced only 0.545 Å ($Q_{\mathrm{max}} = 11.85$ amu$^{1/2}$Å) in PBE0$_{1/3}$/CM; we conclude that the CM is not large enough to accommodate the strain field associated with the displaced Tl resulting in destabilization due to compression against the hard wall of the fixed outer shell of the CM. This conclusion is somewhat counterintuitive since the CM actually has more atoms than the PWM (136 compared to 64). However, fewer of the atoms can move in the CM (52 compared to 64). Additionally, the periodic boundary conditions of the PWM are more flexible than the fixed boundary conditions of the CM. For example, in the PWM, the displacements along the (111) column that contains the Tl are all non-zero (with the second-neighbor Na atoms moving perpendicular to the column). In contrast, in the CM all (both) the Na in the (111) column containing Tl are fixed, constraining the near-neighbor I atoms more in the CM than in the PWM.
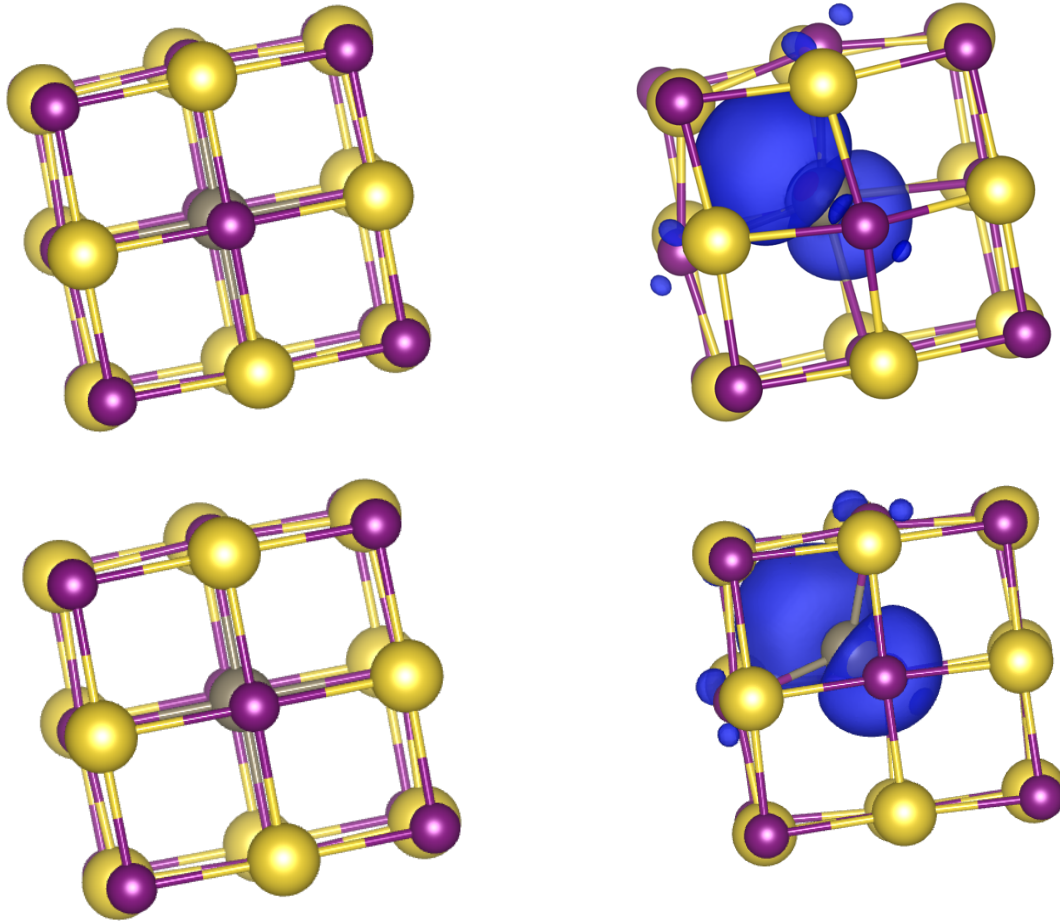
Figure 2. Calculated local environment of a Tl dopant in NaI using the PBE0$_{1/3}$ exchange-correlation approximation in plane-wave (top row) and cluster (bottom row) models without (left column) and with (right column) a trapped electron. The spin density isosurfaces (at 0.001 electrons per cubic angstrom) associated with the trapped electron is plotted in blue. Na atoms are shown in gold, I atoms in purple, and the Tl dopant is grey.

Our previous work on this system [69] used the same CMs employed here to model self-trapped exciton migration in pure NaI. That work used the Becke half-and-half [81,82] (BHH) xc functional ($\alpha = 1/2$) and found good agreement for predicted absorption and emission energies for the self-trapped exciton. We also computed the electron trapping using BHH/CMs. We found

Q_{max}=12.07 using BHH/CMs. Some other exchange-correlation functionals were also explored; results are listed in Table 1. We speculate that the off-center displacement of the Tl and resulting compressive forces upon electron trapping are more difficult to accommodate in CMs than the tensile forces that result when an exciton self-traps. Simulating the self-trapped exciton using PWMs is beyond the scope of the current work but certainly a worthy objective to investigate convergence with respect to model size, which remains an important issue for calculations requiring hybrid xc functionals. The local coordination environment of the Tl in the ground state and trapped electron structures is depicted in Figure 2.

Table 1. Distance along effective phonon coordinate Eq. (4) between Tl-ground-state structure and Tl^0 structure for several xc functionals in CM and PWM calculations.

xc functional	α	Q_{max} PWM (amu$^{1/2}$Å)	Q_{max} CM (amu$^{1/2}$Å)
PBE0 (= PBE0$_{1/4}$)	0.25	–	11.47
HSE06	0.25	11.18	–
PBE0$_{1/3}$	1/3	13.53	11.85
BHH	0.5	–	12.07
HF	1	–	12.77

We then linearly interpolated between the ground-state and trapped electron structures to produce a sequence of structures between $Q = 0$ and $Q = Q_{max}$ and performed single-point energy calculations starting from orbitals derived from either the Tl^0 state or the Tl-ground-state structure. In both cases the extra electron was included. The results of this procedure produce the cc-diagram, plotted in Figure 3 for a variety of approximations. These results show that the trap depth is sensitive to both the exchange-correlation approximation and the type of model (CM or PWM) used. Achieving the same trap depth in a CM as a PWM requires larger α. While we

calculated rough configuration-coordinate diagrams for a variety of DFT approximations, we
only carried out the trapping rate calculations for PBE0$_{1/3}$ using the PWM.
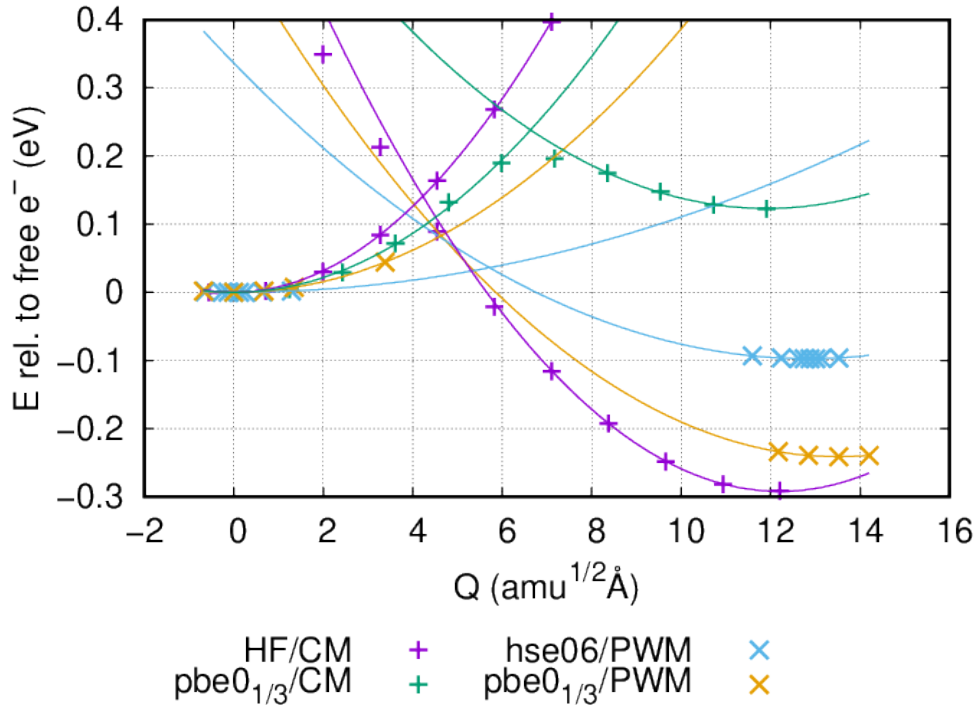

Figure 3. Configuration coordinate diagram calculated using either cluster models (+'s) or
periodic boundary conditions (x's) and HF (black), HSE06 (blue), or PBE0$_{1/3}$ (yellow and
green). The origin of the energy scale is the energy of a free electron in the ground-state Tl$^+$
structure, and the abscissa is Q, the effective 1-D phonon coordinate. Solid lines are quadratic
fits near the appropriate minimum. See the text for details.

C.   Vibrational levels and wavefunctions

With the relevant vibrational dynamics around the Tl center described by an effective 1-D
Schrödinger equation, the task of finding the vibrational structure is equivalent to finding the
rotationless states of a single diatomic molecule (with Q taking the place of the bond length and
the effective 1-D PES taking the place of the interatomic potential in the radial Schrödinger
equation). To compute the vibrational levels and wavefunctions for the motion of the effective

phonon coordinate Q, we used the LEVEL [83] program by LeRoy, which is based on software originally written by Zare [84] for finding the rovibrational levels of diatomic molecules. The eigenvalues are searched for by integrating solutions from the classically forbidden regions at high and low Q towards each other and adjusting the eigenvalue to eliminate the discontinuity in the slope where the two solutions meet. When an eigenvalue is found that supports a smooth solution to the 1-D Schrödinger equation satisfying the boundary conditions on both sides of the classically allowed region, the solution is tabulated, and the code starts searching for a higher eigenvalue or stops if enough solutions have been found.

This approach requires the values of the PES's well into the classically forbidden region, so the computed ab initio points were extended to high and low Q as follows. First, the crystal symmetry implies that the 1-D PES's for the trapped and free states are symmetric about $Q = 0$ (with motion in the positive and negative directions moving to Tl^0 states with Tl displacements along two equivalent [111] directions). Hence reflections through $Q = 0$ of the directly computed points on each PES were added. The free state was well fit by a parabola which was used as the final PES at all Q. For the trapped state, a finely sampled PES in the range of the directly calculated points was generated by interpolation via a cubic spline. The Tl^0 PES was extended beyond the computed data by a parabolic fit determined by the last 3 points. This procedure results in a double-well trapped PES that is symmetric about $Q = 0$ and has continuous derivatives up to the second one. The final PES's are displayed in Figure 4.

The vibrational levels (labelled by the single quantum number $v \geq 0$) belonging to the trapped and free PES's were then found numerically. The reflection symmetry implies that the levels can be classified by parity with the wavefunction for each state having zero in either the function value (v odd) or the first derivative (v even) at $Q = 0$. We searched for solutions starting

with the correct behavior at $Q = 0$ with various trial eigenvalues until all the symmetric and antisymmetric levels were found. A horizontal line between the classical turning points in the harmonic approximation is drawn at the vertical coordinate corresponding to the eigenvalue of every 20th level beyond $v = 2$ for both the trapped and free surfaces is included in Figure 4. The final calculations presented here considered 297 vibrational levels of the trapped PES spanning 0.84 eV. The free electron state was described with 201 vibrational levels spanning 1.15 eV. The harmonic level spacing in the free state is 45.8 cm^{-1} (5.68 meV) and falls in the upper part of the acoustic modes of the NaI host material, consistent with the large mass of Tl compared to the Na that it substitutes. The deep levels of the trapped PES are doubly degenerate and have spacings around 23.4 8 cm^{-1} (2.91 meV), while the levels above the barrier have close to the same spacing corresponding to the combination of the two separate wells to form one large well with twice the width.
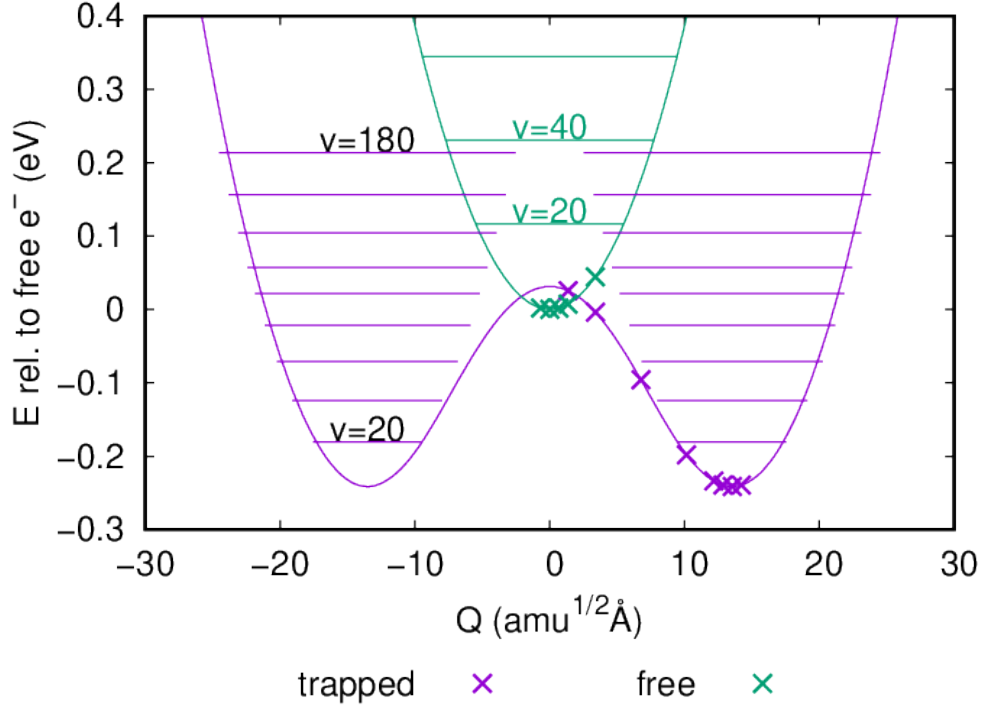
Figure 4. Final configuration-coordinate diagram used for calculation of the vibrational structure. The x's mark explicitly calculated points (and agree with the green x's in Figure 3), the curved solid lines are the interpolated/extrapolated adiabatic potential energy surfaces, and the horizontal solid lines mark every 20th vibrational level (excluding the $v = 0$ levels for clarity), drawn between the classical turning points in the harmonic approximation.

With the vibrational wavefunctions determined for both states, the matrix elements $\langle I|Q|F \rangle$ appearing in Eq. (2) were determined using numerical quadrature. Since the upper PES is a parabola, the corresponding vibrational wavefunctions are the well-known harmonic oscillator functions, which are expressible analytically. However, we treated them numerically using the same procedures for both the upper and lower PES's. As a check on the LEVEL solver, we compared the first few wavefunctions to the expected harmonic oscillator functions and found excellent agreement. Since Q is an odd operator, $\langle I|Q|F \rangle$ vanishes unless $|I\rangle$ and $|F\rangle$ are of

opposite parity. We chose to evaluate all the matrix elements, using this parity selection rule as a post hoc numerical check. In our calculations the ratio of nearby allowed and forbidden matrix elements is around 10^9 (or 18 orders of magnitude in the transition rate, which is proportional to the square of the matrix element).

D. Electron-phonon coupling

The final ingredient needed to evaluate the transition rates is the electron-phonon coupling of Eq. (3). As stated above, these calculations were done using CMs. Two quantities are needed to evaluate Eq. (3): the eigenvalues of the initial and final electron orbitals in the trapped state and the derivative $\left\langle i \middle| \frac{\partial f}{\partial Q} \right\rangle$. We modified the NWChem implementation of the frontier molecular orbital electron transfer approach of Farazdel et al. [85] to compute the derivative $\left\langle i \middle| \frac{\partial f}{\partial Q} \right\rangle$. In calculations using local basis sets, the bases are generally non-orthogonal so that the overlap between two orbitals $\langle i | f \rangle$ is computed using $\langle i | f \rangle = c_i^\dagger S c_f$ where c_i and c_f are column vectors of coefficients describing the orbitals in the basis, and S is the overlap matrix, which coincides with the identity matrix for orthanormal bases. To estimate the derivative $\left\langle i \middle| \frac{\partial f}{\partial Q} \right\rangle$ using finite differences, we constructed a combined geometry in which every atom appears twice: once at the position corresponding to $Q = Q_{\max}$ and once at the (possibly identical) position corresponding to $Q = Q_{\max} + \delta Q$. The basis sets were similarly combined. The overlap matrix of the combined geometry (which is now of twice the rank of the original overlap matrices) was then generated. Overlaps between orbitals expressed in either geometry could then be found by using the appropriate block of the combined overlap matrix. We used $\delta Q = -Q_{\max}/100$. The initial and final electronic orbitals $|i\rangle$ and $|f\rangle$ must be determined. The orbital occupied by the trapped electron is obvious since the motion of the Tl from its equilibrium Tl^+ position to the Tl^0

19

minimum pulls a single occupied Tl p-orbital well into the gap. The symmetry-breaking of the Tl

displacement stabilizes the trapping orbital with lobes along the soft [111] direction of NaI,

leading to a sensitive dependence of the trapping orbital shape on Q and a correspondingly large

$\left\langle i \left| \frac{\partial f}{\partial Q} \right\rangle\right.$ reflecting the strong interaction between electrons in this orbital and the lattice vibrations.

This strong interaction explains why Tl is an effective electron trap in NaI:Tl. This strong

trapping behavior allows Tl to outcompete other (optically inactive) traps present in NaI, which

leads to the high light yield of NaI:Tl. The choice of the free electron orbital is more arbitrary.

We choose the conduction band minimum orbital to describe the free electron. This orbital is

comprised primarily by the s-orbitals of the Na atoms in the second coordination shell of the Tl.

For the case of trapping thermalized free electrons the appropriate initial state to consider is a

thermal ensemble of the empty states $|iI\rangle$. The CBM orbital is the only one with appreciable

electron-phonon coupling W_{if} within several $k_B T$ of the CBM at room temperature. In the case of

detrapping, the initial state is a thermal population of the levels of trapped double-well potential

shown in Figure 4. For transitions to occur, then, there must be thermal population of a

vibrational state of the trapped PES with energy at least as large as the ground vibrational state of

the final electronic state. Figure 5 shows the density of states (DOS) from the region near the

CBM (in both computational settings) along with sticks to indicate the strength of the electron-

phonon coupling of each state. Most of the unoccupied electronic states have small couplings

because the orbitals do not involve the Tl or neighboring atoms and hence have little overlap

with the trapping Tl p-orbital. In both cases (trapping and detrapping), then, we expect the CBM

orbital to be the dominant upper electronic level. Hence, the capture and release coefficients

presented below consider only transitions between the trapping Tl p-orbital and the CBM orbital.

Our calculation gives $W_{if} = 1.08 \times 10^{-3}$ eV $\cdot$AMU$^{1/2} \cdot$ Å for the electronic matrix element between the trapping orbital and the CBM.
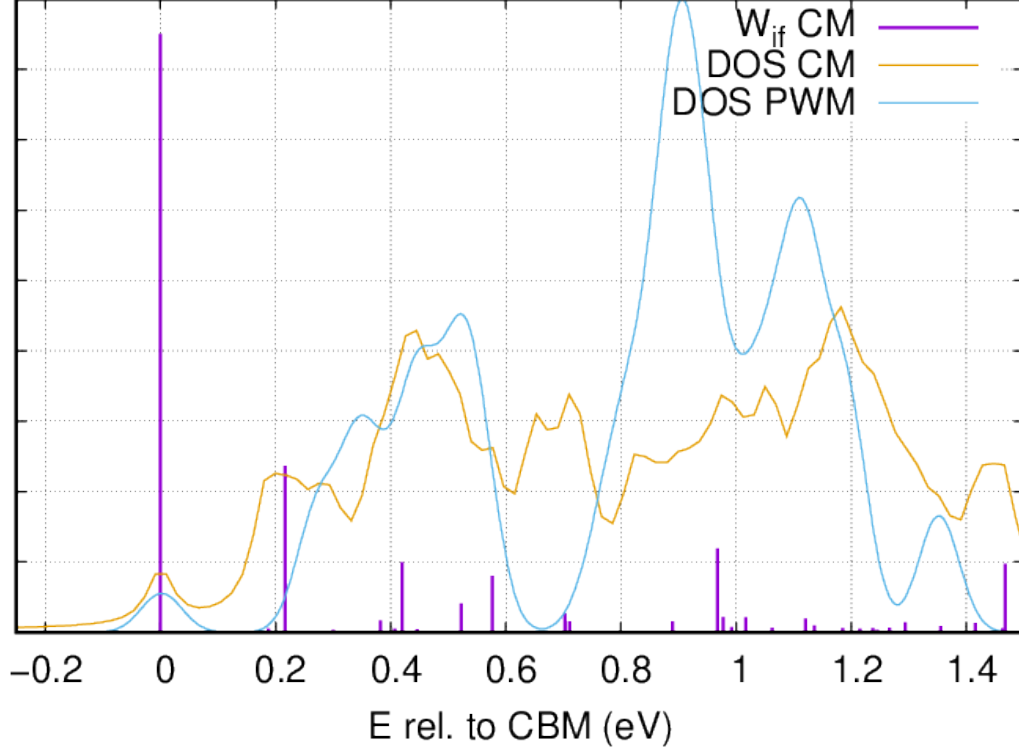

Figure 5. Electron-phonon matrix elements and density of states from CM calculations and density of states from PWM calculations near the conduction band minimum.

E.   Electron capture and release rates

The combination $\sum_I w_I^i \sum_F |\langle I|Q|F\rangle|^2 \delta(E_{iI} - E_{fF})$ was constructed as a function of T (which enters only through the thermal occupation factors w_I^i, which in turn were computed by direct summation of the vibrational partition function at each T over the available vibrational states) for trapping and detrapping cases. The δ-function was approximated by a Gaussian of FWHM 2.5 meV; the final release rates were tested to make sure they did not depend sensitively on the width. The final release rate and electron capture coefficient were then simply obtained from Eq. (5). These quantities are the primary result of this work and are plotted in Figure 6, where they

are compared to available data from the analysis of thermally stimulated luminescence (TSL) experiments [5,51] and of a kinetic Monte Carlo model of scintillation [33] fitted to scintillation decay curves. To explore the sensitivity of these calculations to errors in the electronic structure, we have plotted results obtained by shifting the trap depth up and down by 0.1 eV (an arbitrary value that we believe is larger than the actual error). This exercise shows that the results are especially sensitive to shifts towards deeper a deeper trap ($\delta E < 0$) which lower both capture and release rates by more than four orders of magnitude over the entire temperature range considered.
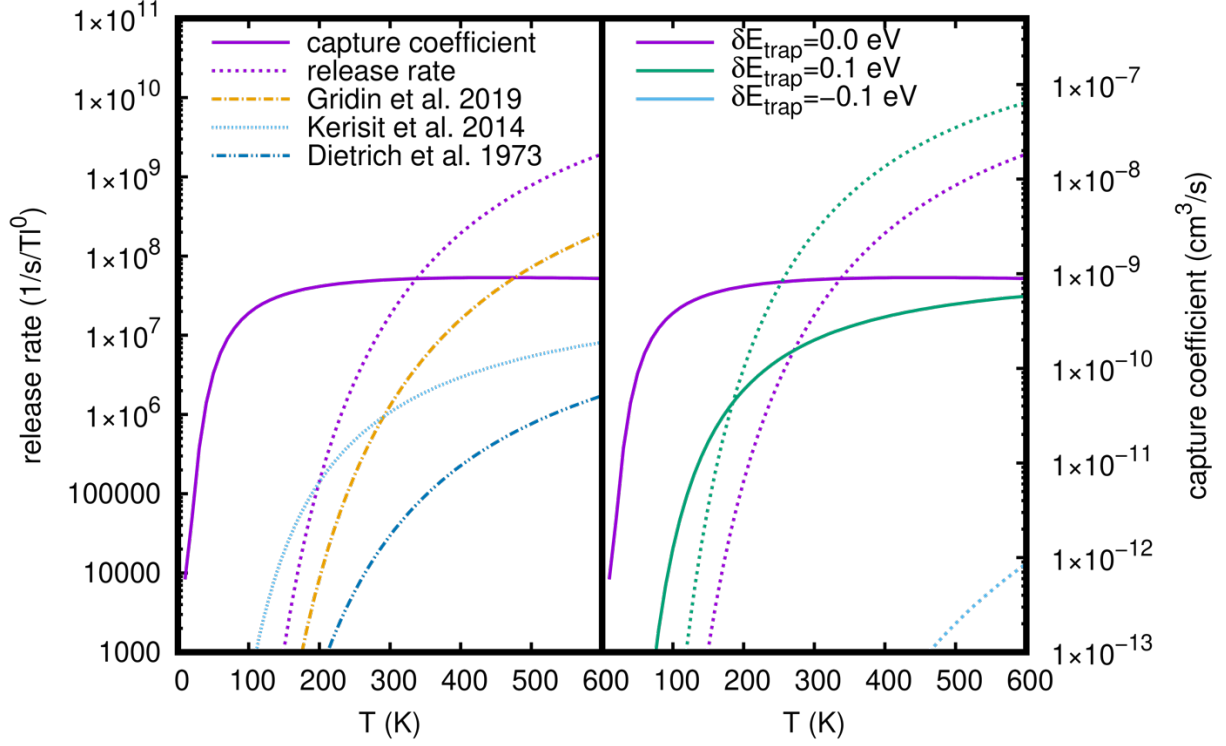
Figure 6. Capture coefficient (solid lines) and release rate (broken lines) as a function of temperature. The calculated values, shown in both panels, are in black. In the left panel the theoretical release rate (dotted purple) is compared to Arrhenius curves from thermally stimulated luminescence measurements by Dietrich et al. [5] and Gridin et al. [51] as well as an Arrhenius curve resulting from analysis of scintillation decay curves by Kerisit et al. [33]. In the right panel, our predictions (purple) are compared to values that we would obtain if the trapped state was shifted by $\delta E = 0.1$ eV (green) or $\delta E = -0.1$ eV (blue) in energy. The capture rate for $\delta E = -0.1$ eV is below the bottom of graph.

Release

The calculated release rate exhibits approximately Arrhenius behavior. A fit of the curve to Ae^{-E/k_BT} yields $A = (2.37 \pm 0.01) \times 10^{11}\text{s}^{-1}$ and $E = 0.2450 \pm 0.0001$ eV. The latter is close to, but does not agree with, either the trap depth (0.242 eV) or the energy difference between the ground vibrational states of the trapped and free PES's (0.241 eV). This is a textbook thermally activated process: as the temperature is raised, detrapping commences when there is thermal population in trapped states of high enough energy to transition into the ground vibrational state of the Tl^+ configuration. We also note that the shape of the lower (Tl^0) PES, which results from the soft nature of the crystal, has a large effect on the magnitude of the release rates, which is determined by the tail of the vibrational wavefunctions that extends to near $Q = 0$, where the low-lying Tl^+ state wave functions are non-vanishing. Hence, calculations done in the harmonic approximation, including Refs. [52,53] and all other theoretical works that we are aware of, will badly underestimate the rates in situations such as this one.

The comparison of the release rate to the thermally stimulated luminescence experiments deserves comment. These experiments are performed by subjecting the cold (T~10 K) sample to x-rays to develop an initial population of trapped excitations followed by gradual heating. As the sample warms, thermal detrapping occurs leading to luminescence, which is measured. There is large discrepancy in the release rates reported in Refs. [5] and [51], with Gridin's larger release rates (green dash-dot trace in Figure 6) much closer to the theoretical calculations of this work (yellow dots). As discussed in detail by Gridin, the difference between these curves stems not from differences in the measured luminescence, but in the method of analysis. In fact, Gridin presents two analyses in Ref. [51]. The first uses the same analysis method as Ref. [5], which consists of fitting the initial rise of the glow peak resulting from electron release from Tl^0 to the

Arrhenius form. The second analysis of Gridin, et al. is based on a more sophisticated model that uses data from the entire glow peak. Based on simulations of the TSL curves for NaI doped with three different activators, Gridin et al. deem their estimates to be some of the most reliable experimental determinations available for thermal release of electrons form Tl^0 in NaI. Our theoretical simulations agree well with Refs. [5,51] with regards to the shape of the release vs. T curve (i.e., Arrhenius behavior with a trap depth near 0.26 eV). The magnitudes of the theoretical release rates presented here are greater than the best available experimental estimates by a factor of 'only' around 14. Given that slight differences in the TSL analysis changes the magnitude of the release rate by a factor of approximately 44, we consider the agreement with whole-peak fitting procedure of Ref. [51] to be fairly good. It appears that the experimental and theoretical pictures are converging.

Capture

In contrast to the release processes, which are very well described by the Arrhenius equation, the capture coefficient arising from our theoretical treatment is not. In fact, the capture coefficient curve (solid purple line in Figure 5) exhibits a maximum around $T = 450$ K, decreasing at higher temperatures. Even at practically relevant temperatures for gamma-ray detection (i.e. room temperature), our predicted capture coefficient is around 10% lower than suggested by an Arrhenius fit (presented in Figure 7). We carefully checked that this effect is not a reflection of unconverged calculations. For example, removing the highest 100 vibrational levels of the Tl^0 state (the final states for the capture transition) results in a decrease of the calculated capture rate at $T = 1000$ K of less than 1%.
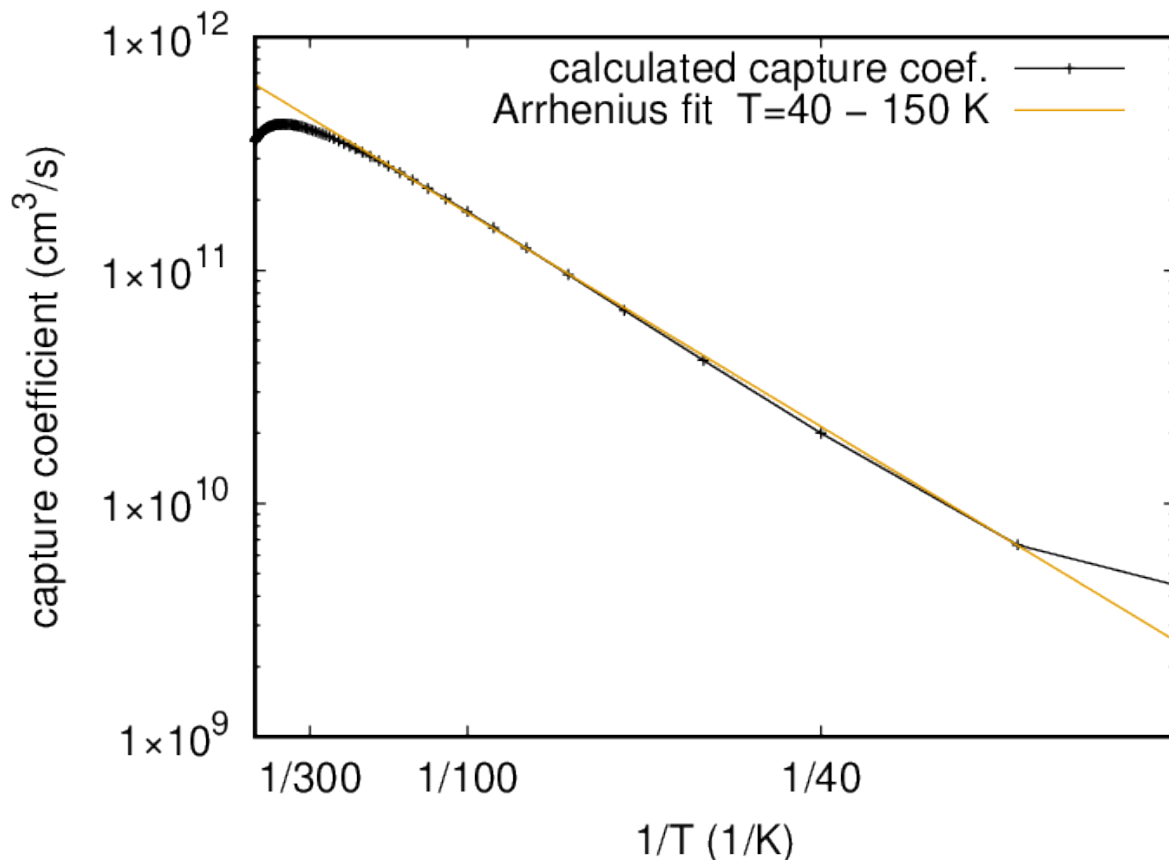
Figure 7. Arrhenius fit (yellow line) to calculated capture coefficient (decorated black curve – same data as the solid purple curve in Figure 6).

The origin of the suppression of capture at high temperatures turns out to be a kind of anharmonic effect arising from resonance of the vibrational states from the double-well Tl^0 PES with the thermally occupied levels of the Tl^+ upper state. Figure 8 shows color intensity plots of the transition strengths $|\langle I|Q|F\rangle|^2$. The top panel shows all the states considered; the bottom panel is zoomed into the region of phase space in which the transitions occur.
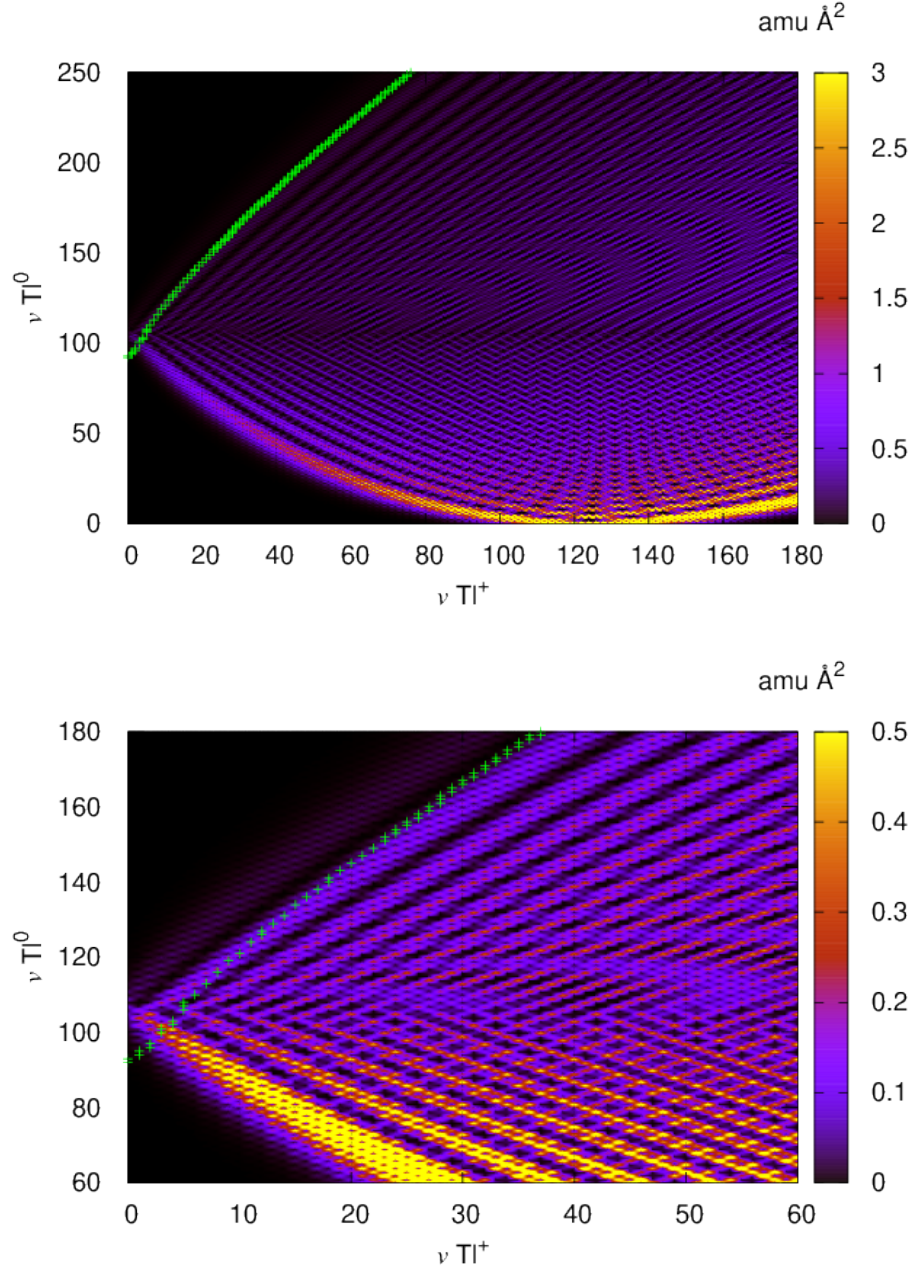
Figure 8. Heat map of the squared matrix elements $|\langle I|Q|F\rangle|^2$ between different vibrational states of the upper (horizontal axis) and lower (vertical axis) PES's. The green +'s mark transitions that are allowed by energy conservation. Since none of the plotted quantities involve the thermal occupation factors, this figure describes both trapping and detrapping probabilities.

The double-well structure of the lower PES leads to interesting patterns in Figure 8. States of the lower (Tl^0) PES with $v < 92$ have eigenvalues below the barrier between the two wells, and there is a region around $Q = 0$ that is classically forbidden for these states. Higher lying states have no classically forbidden region between the two wells and are separated in Figure 8 from the lower lying states by a dark band. The fine checkerboard pattern evident in the bottom panel results from the parity selection rule discussed above. The energy conserving δ-function of Eq. (5) is satisfied for pairs of upper and lower states marked with green +'s in Figure 8. Efficient trapping occurs between pairs of states that have large transition strengths (indicated by the color scale) and fall on the line of green +'s. So far, our discussion of Figure 8 applies equally to trapping and detrapping. The temperature dependence of the capture rates in our supercell (and hence the final capture coefficient) arises from the thermal populations of the upper states, which correspond to the horizontal axis in Figure 8. The strongest transitions that conserve energy have low vibrational quantum numbers in the upper state. As the temperature is increased, the thermal occupation of these states is lowered as they lose occupancy to higher-lying states that are inaccessible at low T.

Figure 8 clearly shows that fine details of the PES's (e.g., the height of the barrier of the lower PES relative to the minimum of upper state) determine the temperature dependence of the transition rates through a complicated interplay between the matrix elements and the locus of energy conserving transitions. Figure 3 clearly shows that such details of the cc-diagram are quite sensitive to xc approximation used, underlying the need to have a good description of the energetics of both initial and final states for the type of simulations presented here. The right-hand panel of Figure 6 can be interpreted in terms of Figure 8. Errors in the trap depth shift the locus of energy-conserving transitions up for shallower traps and down for deeper traps. In

particular, the decrease in capture rate as the trapped state is raised toward the CBM can be understood by noting that shifting the green +s up in Figure 8 moves them over less intense parts of the color map.

V.   CONCLUSIONS

We have used state-of-the-art hybrid density functional theory electronic structure methods, capable of reliably representing both extended and localized electronic states, to explore the adiabatic PES's involved in transitions of the charge state of Tl dopants in NaI:Tl. Due to the soft nature of NaI, we have found significant departures from harmonic behavior. Numerical methods from gas phase diatomic spectroscopy have been adapted to the current problem, yielding a method that can treat PES's of arbitrary shape. We have implemented a method to estimate the electron-phonon coupling using a local-orbital description of the electronic states involved in trapping and detrapping of electrons on Tl sites. From these ingredients, we have calculated trapping and detrapping rates in agreement with available data. Our numerical calculations elucidate the manner in which the symmetry of the trapping orbital interacts with the facile motion of the Tl to produce efficient trapping centers that make NaI:Tl a bright scintillator. We predict, surprisingly, that the capture rate for electrons should decrease as T is raised above 450 K. The success of this work shows that modern electronic structure methods have the capacity, if used carefully, to treat delicate problems of microscopic dynamics following excitation, yielding information that is difficult to access experimentally.

---

[1]   G. F. Knoll, *Radiation Detection and Measurement* (Wiley, 2000).

[2]   R. Hofstadter and M. H. Stein, IEEE TNS **22**, 13 (1975).

[3]   R. W. Birkmire, R. B. Murray, and M. Luntz, Phys. Rev. B **15**, 31 (1977).

[4]   H. B. Dietrich and R. B. Murray, J. Lumin. **5**, 155 (1972).

[5]   H. B. Dietrich, A. E. Purdy, R. B. Murray, and R. T. Williams, Phys. Rev. B **8**, 5894 (1973).

[6]   F. J. Keller and R. B. Murray, Phys. Rev. **150**, 670 (1966).

[7]   R. B. Murray, IEEE TNS **Ns22**, 54 (1975).

[8]   R. B. Murray and F. J. Keller, Phys. Rev. **137**, A942 (1965).

[9]   R. D. Popp and R. B. Murray, Journal of Physics and Chemistry of Solids **33**, 601 (1972).

[10]   R. G. Fuller, R. T. Williams, and M. N. Kabler, Phys. Rev. Lett. **25**, 446 (1970).

[11]   R. T. Williams and M. N. Kabler, Phys. Rev. B **9**, 1897 (1974).

[12]   R. T. Williams and K. S. Song, Journal of Physics and Chemistry of Solids **51**, 679 (1990).

[13]   R. T. Williams, K. S. Song, W. L. Faust, and C. H. Leung, Physical Review B **33**, 7232 (1986).

[14]   G. Bizarri, N. J. Cherepy, W. S. Choong, G. Hull, W. W. Moses, S. A. Payne, J. Singh, J. D. Valentine, A. N. Vasilev, and R. T. Williams, IEEE Transactions on Nuclear Science **56**, 2313 (2009).

[15]   G. Bizarri, W. W. Moses, J. Singh, A. N. Vasil'ev, and R. T. Williams, Journal of Luminescence **129**, 1790 (2009).

[16]   G. Bizarri, W. W. Moses, J. Singh, A. N. Vasil'Ev, and R. T. Williams, Journal of Applied Physics **105**, 44507 (2009).

[17]   G. Bizarri, W. W. Moses, J. Singh, A. N. Vasil'Ev, and R. T. Williams, Physica Status Solidi (C) Current Topics in Solid State Physics **6**, 97 (2009).

[18]   J. Q. Grim, Q. Li, K. B. Ucer, A. Burger, G. A. Bizarri, W. W. Moses, and R. T. Williams, Physica Status Solidi (A) Applications and Materials Science **209**, 2421 (2012).

[19]   J. Q. Grim, K. B. Ucer, A. Burger, P. Bhattacharya, E. Tupitsyn, E. Rowe, V. M. Buliga, L. Trefilova, A. Gektin, G. A. Bizarri, W. W. Moses, and R. T. Williams, Physical Review B - Condensed Matter and Materials Physics **87**, 125117 (2013).

[20]   H. Huang, Q. Li, X. Lu, Y. Qian, Y. Wu, and R. T. Williams, Physica Status Solidi - Rapid Research Letters **10**, 762 (2016).

[21]   M. Prange, D. Wu, Y. Xie, L. W. Campbell, F. Gao, and S. Kerisit, Proceedings of SPIE **9213**, 92130L (2014).

[22]   Q. Li, J. Q. Grim, K. B. Ucer, A. Burger, G. A. Bizarri, W. W. Moses, and R. T. Williams, Physica Status Solidi - Rapid Research Letters **6**, 346 (2012).

[23]   Q. Li, J. Q. Grim, R. T. Williams, G. A. Bizarri, and W. W. Moses, Nuclear Instruments and Methods in Physics Research, Section A: Accelerators, Spectrometers, Detectors and Associated Equipment **652**, 288 (2011).

[24]   Q. Li, J. Q. Grim, R. T. Williams, G. A. Bizarri, and W. W. Moses, Journal of Applied Physics **109**, 123716 (2011).

[25]   Q. Li, R. T. Williams, and D. berg, Physica Status Solidi (B) Basic Research **250**, 233 (2013).

[26]   X. Lu, Q. Li, G. A. Bizarri, K. Yang, M. R. Mayhugh, P. R. Menge, and R. T. Williams, Physical Review B - Condensed Matter and Materials Physics **92**, 115207 (2015).

[27]   W. W. Moses, G. A. Bizarri, R. T. Williams, S. A. Payne, A. N. Vasil'Ev, J. Singh, Q. Li, J. Q. Grim, and W. S. Choong, IEEE Transactions on Nuclear Science **59**, 2038 (2012).

[28]   V. Pankratov, A. I. Popov, L. Shirmane, A. Kotlov, G. A. Bizarri, A. Burger, P. Bhattacharya, E. Tupitsyn, E. Rowe, V. M. Buliga, and R. T. Williams, Radiation Measurements **56**, 13 (2013).

[29]   K. B. Ucer, G. Bizarri, A. Burger, A. Gektin, L. Trefilova, and R. T. Williams, Physical Review B - Condensed Matter and Materials Physics **89**, 165112 (2014).

[30]   R. T. Williams, J. Q. Grim, Q. Li, K. B. Ucer, G. A. Bizarri, and A. Burger, Springer Series in Materials Science **203**, 299 (2015).

[31]   R. T. Williams, J. Q. Grim, Q. Li, K. B. Ucer, and W. W. Moses, Physica Status Solidi (B) Basic Research **248**, 426 (2011).

[32]   S. Kerisit, K. M. Rosso, B. D. Cannon, F. Gao, and Y. Xie, Journal of Applied Physics **105**, 114915 (2009).

[33]   S. Kerisit, Z. G. Wang, R. T. Williams, J. Q. Grim, and F. Gao, IEEE TNS **61**, 860 (2014).

[34]   S. Kerisit, K. M. Rosso, and B. D. Cannon, IEEE TNS **55**, 1251 (2008).

[35]   M. P. Prange, L. W. Campbell, and S. Kerisit, Phys. Rev. B **96**, 104307 (2017).

[36]   M. P. Prange, L. W. Campbell, D. Wu, F. Gao, and S. Kerisit, Physical Review B - Condensed Matter and Materials Physics **91**, 104305 (2015).

[37]   A. N. Vasil'Ev and A. V. Gektin, IEEE Transactions on Nuclear Science **61**, 235 (2014).

[38]   M. P. Prange, Y. Xie, L. W. Campbell, F. Gao, and S. Kerisit, Journal of Applied Physics **122** (2017).

[39]   R. Devanathan, L. R. Corrales, F. Gao, and W. J. Weber, Nucl Instrum Meth A **565**, 637 (2006).

[40]   S. A. Payne, N. J. Cherepy, G. Hull, J. D. Valentine, W. W. Moses, and W.-S. Choong, IEEE Transactions on Nuclear Science **56**, 2506 (2009).

[41]   R. Lapin, M. L. Kamath, J. Engler, and H. Friedman, Am J Gastroenterol **61**, 185 (1974).

[42]   S. Lam, S. E. Swider, A. Datta, and S. Motakef, IEEE TNS **62**, 3397 (2015).

[43]   K. Yang and P. R. Menge, J. Appl. Phys. **118**, 213106 (2015).

[44]   N. V. Shiran, A. V. Gektin, Y. Boyarintseva, S. Vasyukov, A. Boyarintsev, V. Pedash, S. Tkachenko, O. Zelenskaya, N. Kosinov, O. Kisil, and L. Philippovich, IEEE TNS **57**, 1233 (2010).

[45]   T. Shalapska, F. Moretti, E. Bourret, and G. Bizarri, J. Lumin. **202**, 497 (2018).

[46]   I. V. Khodyuk, S. A. Messina, T. J. Hayden, E. D. Bourret, and G. A. Bizarri, J. Appl. Phys. **118**, 084901 (2015).

[47]   A. V. Gektin, A. N. Belsky, and A. N. Vasil'ev, IEEE TNS **61**, 262 (2014).

[48]   Q. G. Feng and K. Biswas, J. Appl. Phys. **120**, 213104 (2016).

[49]   R. H. Bartram, L. A. Kappers, D. S. Hamilton, A. Lempicki, C. Brecher, V. Gaysinskiy, E. E. Ovechkina, and V. V. Nagarkar, IEEE TNS **55**, 1232 (2008).

[50]   M. S. Alekhin, J. T. M. de Haas, I. V. Khodyuk, K. W. Krämer, P. R. Menge, V. Ouspenski, and P. Dorenbos, Appl. Phys. Lett. **102**, 161915 (2013).

[51]   S. Gridin, R. T. Williams, A. Belsky, E. Galenin, A. Gektin, N. Shiran, S. Vasiukov, and A. Vasil'ev, J. Phys. Chem. C **123**, 13519 (2019).

[52]   A. Alkauskas and Q. a. Yan, Physical Review B - Condensed Matter and Materials Physics **90** (2014).

[53]   G. D. Barmparis, Y. S. Puzyrev, X. G. Zhang, and S. T. Pantelides, Physical Review B - Condensed Matter and Materials Physics **92**, 214111 (2015).

[54]   L. Shi, K. Xu, and L. W. Wang, Phys. Rev. B **91** (2015).

[55]   L. Shi, K. Xu, and L. W. Wang, Phys. Rev. B **97** (2018).

[56]   P. A. M. Dirac, Proceedings of the Royal Society A: Mathematical, Physical and Engineering Sciences **114**, 243 (1927).

[57]   G. D. Mahan, *Many-Particle Physics* (Springer, 2000), Physics of Solids and Liquids.

[58]   M. G. Burt, Journal of Physics C: Solid State Physics **16**, 4137 (1983).

[59]   A. Alkauskas, J. L. Lyons, and D. a. Steiauf, Physical Review Letters **109** (2012).

[60]   G. Kresse and J. Furthmller, Physical Review B - Condensed Matter and Materials Physics **54**, 11169 (1996).

[61]   G. Kresse and J. Furthmuller, Computational Materials Science **6**, 15 (1996).

[62]   G. Kresse and J. Hafner, Phys. Rev. B **47**, 558 (1993).

[63]   G. Kresse and J. Hafner, Phys Rev B Condens Matter **49**, 14251 (1994).

[64]   P. E. Blochl, Phys Rev B Condens Matter **50**, 17953 (1994).

[65]   G. Kresse and D. Joubert, Physical Review B **59**, 1758 (1999).

[66]   W. S. Choong, G. Bizarri, N. J. Cherepy, G. Hull, W. W. Moses, and S. A. Payne, Nucl Instrum Meth A **646**, 95 (2011).

[67]   J. S. Schweitzer and W. Ziehl, IEEE TNS **30**, 380 (1983).

[68]   M. Valiev, E. J. Bylaska, N. Govind, K. Kowalski, and T. P. a. Straatsma, Computer Physics Communications **181**, 1477 (2010).

[69]   M. P. a. Prange, Physical Review B - Condensed Matter and Materials Physics **87**, 115101 (2013).

[70]   N. Govind, P. V. Sushko, W. P. Hess, M. Valiev, and K. Kowalski, Chemical Physics Letters **470**, 353 (2009).

[71]   L. F. Pacios and P. A. Christiansen, The Journal of Chemical Physics **82**, 2664 (1985).

[72]   M. M. Hurley, L. F. Pacios, P. A. Christiansen, R. B. Ross, and W. C. Ermler, The Journal of Chemical Physics **84**, 6840 (1986).

[73]   F. Weigend and R. Ahlrichs, Physical Chemistry Chemical Physics **7**, 3297 (2005).

[74]   J. P. Perdew, K. Burke, and M. Ernzerhof, Physical Review Letters **77**, 3865 (1996).

[75]   J. P. Perdew, M. Ernzerhof, and K. Burke, The Journal of Chemical Physics **105**, 9982 (1996).

[76]   C. Adamo and V. Barone, Journal of Chemical Physics **110**, 6158 (1999).

[77]   P. Cortona, J. Chem. Phys. **136**, 086101 (2012).

[78]   C. A. Guido, E. Bremond, C. Adamo, and P. Cortona, J. Chem. Phys. **138**, 021104 (2013).

[79]   F. C. Brown, C. Ghwiller, H. Fujita, A. B. Kunz, W. Scheifley, and N. Carrera, Physical Review B **2**, 2126 (1970).

[80]   R. W. G. Wyckoff, *Crystal Structures* (John Wiley, New York, 1963).

[81]   A. D. Becke, The Journal of Chemical Physics **98**, 5648 (1993).

[82]   A. D. Becke, The Journal of Chemical Physics **98**, 1372 (1993).

[83]   R. J. Le Roy, Journal of Quantitative Spectroscopy and Radiative Transfer **186**, 167 (2017).

[84]   R. N. Zare, The Journal of Chemical Physics **40**, 1934 (1964).

[85]   A. Farazdel, M. Dupuis, E. Clementi, and A. Aviram, J Am Chem Soc **112**, 4206 (1990).